Research Square

Preprints are preliminary reports that have not undergone peer review.
They should not be considered conclusive, used to inform clinical practice,
or referenced by the media as validated information.

Diurnal Tidal Currents in the Gulf of Tonkin and the Qiongzhou Strait: Regime Characterization with Implications for Navigation and Tidal-Stream Energy

Manh Hung Nguyen

hung.nguyenmanh@ut.edu.vn

Ho Chi Minh City University of Transport

Gia Huy Dinh

Ho Chi Minh City University of Transport

Research Article

Keywords: Gulf of Tonkin, diurnal tides, Form Factor, tidal currents, EOT20, standing wave, maritime navigation, tidal-stream energy

Posted Date: July 24th, 2026

DOI: https://doi.org/10.21203/rs.3.rs-10268691/v1

License: This work is licensed under a Creative Commons Attribution 4.0 International License.
Read Full License

Additional Declarations: No competing interests reported.

Diurnal Tidal Currents in the Gulf of Tonkin and the Qiongzhou Strait: Regime Characterization with Implications for Navigation and Tidal-Stream Energy

Manh Hung Nguyen[1*], Gia Huy Dinh[1]

AIT Research Group, University of Transport Ho Chi Minh City, Ho Chi Minh City 70000, Vietnam

** Corresponding author: hung.nguyenmanh@ut.edu.vn*

Abstract

The Gulf of Tonkin has one of the world's most strongly diurnal tidal regimes, yet spatially continuous descriptions of that regime, and of its surface kinetic energy, remain scarce. We combine harmonic synthesis of the EOT20 global tide model, daily GLORYS12 reanalysis currents, hourly CMEMS operational surface currents, ERA5 winds, and tide-gauge records to characterise the diurnal regime and surface current energy of the Gulf. The first spatially continuous Form Factor map for the basin places the F = 3 contour near 19°N, with F reaching 12.7 in the northern interior. Synthesised elevations reproduce hourly records at Hon Dau and Beihai, matching the dominant constituent amplitudes to within seven percent in vector terms, with a Nash–Sutcliffe efficiency of 0.916 at Hon Dau. Mean surface power density is 2.86 W/m² in the daily reanalysis, against 121.35 W/m² for a frictionless progressive-wave scaling of the EOT20 tide, an apparent 42-fold gap. Harmonic analysis of a 365-day hourly record at four sites shows that this gap is not a pointwise frictional ratio: daily averaging alone suppresses power density by factors of 3.8–8.9, while the ratio of scaled to realised tidal amplitude (0.1–2.6) traces the standing-wave structure of the near-resonant diurnal oscillation, with K_1 and O_1 exceeding M_2 at every site. Combined diurnal current amplitudes approach 1.3 m/s near the Qiongzhou Strait, a busy shipping lane and the only part of the Gulf meeting first-order tidal-stream screening thresholds; its single daily high-water cycle shapes both navigation and energy use.

Keywords: Gulf of Tonkin; diurnal tides; Form Factor; tidal currents; EOT20; standing wave; maritime navigation; tidal-stream energy

1 Introduction

Most of the world's shelf seas are dominated by the semi-diurnal lunar tide. The Gulf of Tonkin is one of the few large basins where the opposite holds: the declinational diurnal constituents K_1 and O_1 carry most of the tidal energy, and the principal semi-diurnal constituent M_2 is weak through much of the interior (Fang et al. 1999; Minh et al. 2014). This peculiarity is usually attributed to a near-resonant response of the semi-enclosed basin at diurnal frequencies, a quarter-wavelength oscillation set by the Gulf's length and depth (Zu et al. 2008; Piton et al. 2020). The diurnal character of the Gulf is well established at individual coastal stations, where harmonic constants have been available for decades. What has been missing is a spatially continuous view: a map of the tidal regime classification across the entire basin, and

a consistent picture of how the kinetic energy of surface currents is distributed in space and through the year.

Two families of freely available global products now make such a view possible without running a regional hydrodynamic model. Global tide models, whether data-assimilative (Egbert and Erofeeva 2002) or purely empirical such as EOT20, provide harmonic constants for the major constituents on a 0.125° grid (Hart-Davis et al. 2021), from which elevations and first-order current estimates can be synthesised anywhere in the basin. Ocean reanalyses and operational analyses distributed through the Copernicus Marine Service supply gridded surface currents at daily and hourly resolution (Lellouche et al. 2018). The two sources describe different physics. A tide model isolates the astronomical signal; a reanalysis integrates tidal motion, monsoon-driven circulation, density-driven flow, and eddies into a single velocity field. Their relationship in a strongly diurnal, near-resonant basin has not, to our knowledge, been examined quantitatively, and the relationship between astronomical tidal forcing and the total surface kinetic energy of the Gulf remains poorly constrained.

There is also a practical motive for closing this gap. Vietnam's long coastline has prompted recurring interest in marine renewable energy, and tidal-stream resource screening conventionally begins with maps of current speed and power density (Lewis et al. 2015; IEC 2015). Screening exercises in data-sparse regions often rely on whichever gridded product is at hand, and the choice matters: as we show below, estimates built from a tide model and from a daily reanalysis differ by more than an order of magnitude in the domain mean, for reasons that are physical rather than numerical. The same tidal information underpins maritime navigation: the Gulf carries heavy ship traffic to the port of Hải Phòng and through the Qiongzhou Strait, where tidal range and tidal-stream currents govern the windows for safe transit of deep-draft vessels.

This study characterises the diurnal tidal regime and surface current energy of the Gulf of Tonkin using only open data: EOT20 harmonic constants, GLORYS12 daily reanalysis currents, hourly operational surface currents from the CMEMS global system, ERA5 winds, and hourly tide-gauge records. We construct the first spatially continuous Form Factor map for the basin, validate the synthesised tide against the Hon Dau gauge, map power density from both the tide model and the reanalysis, and then reconcile the two through constituent-level harmonic analysis of an hourly record. The reconciliation produces what we regard as the central physical result of the paper: the ratio between a progressive-wave scaling of the tide-model elevations and the realised tidal current amplitudes is not uniform but spatially organised by the standing-wave structure of the near-resonant diurnal oscillation. The energy-screening implications follow naturally and are treated as a secondary application.

2 Study area

The Gulf of Tonkin (Vietnamese: Vịnh Bắc Bộ; roughly 16.5–22°N, 105.5–111.5°E) is a shallow semi-enclosed basin in the northwestern South China Sea, bounded by the Vietnamese coast to the west, the Chinese mainland to the north, and Hainan Island to the east (Fig. 1). Depths are mostly less than 60 m in the northern half and increase toward the southern entrance, which opens to the South China Sea across a sill of roughly 100 m. A second, much

narrower connection exists in the northeast through the Qiongzhou Strait between Hainan and the Leizhou Peninsula, a channel about 30 km wide and shallower than 50 m that carries a significant exchange flow (Shi et al. 2002). The basin lies under the East Asian monsoon: northeasterly winds prevail from roughly October to March and weaker southwesterlies from June to August, driving a seasonally reversing circulation along the Vietnamese coast (Hu et al. 2000; Gao et al. 2013). Tidal range at the head of the Gulf is among the largest of any diurnal regime, exceeding 4 m at spring tropic tides near Hải Phòng.

Geometrically the basin is elongated, running about 500 km along its northwest–southeast axis and some 250 km across, with a mean depth near 50 m that increases from under 30 m in the shallow north to roughly 100 m at the southern sill. This shallow, semi-enclosed shape, open mainly at the southern entrance, is the physical setting for the near-resonant diurnal response we return to in Sect. 5.1. Freshwater enters chiefly through the Red River system at the northwestern head, adding a seasonal buoyancy forcing that the present barotropic analysis does not treat but that contributes to the circulation captured by the reanalysis.

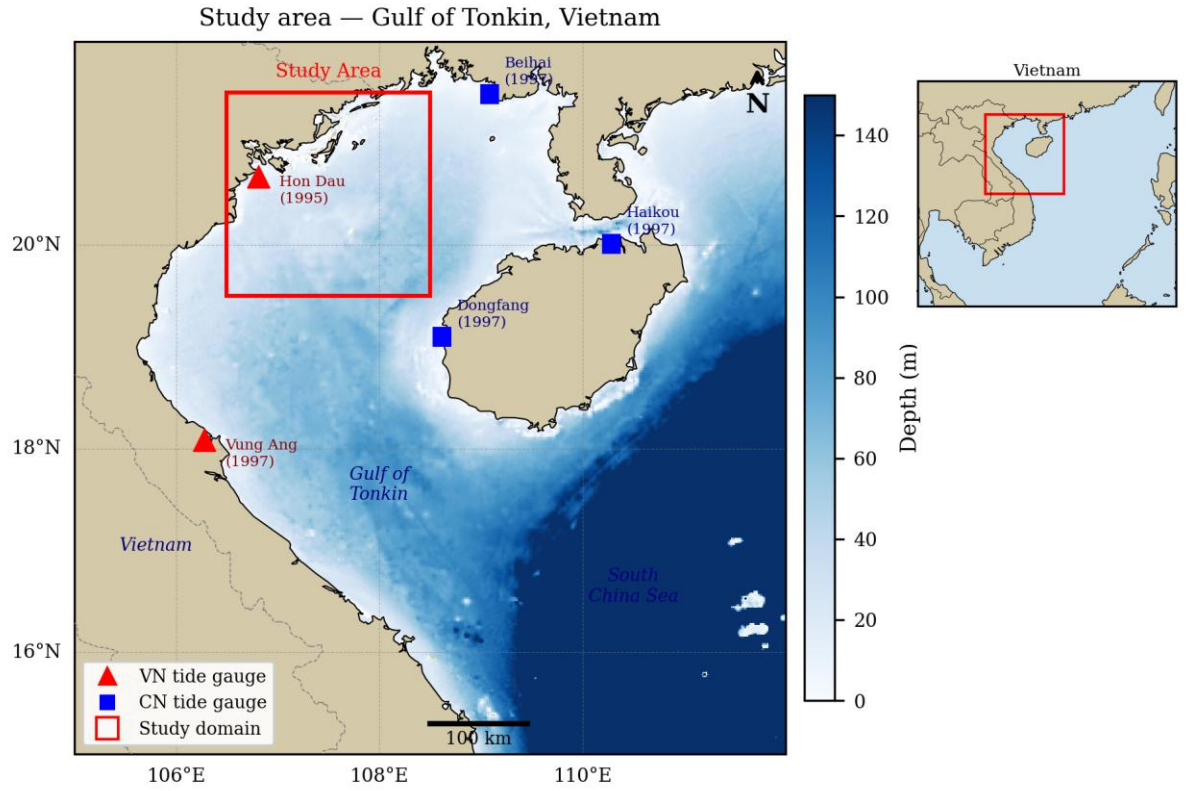

Fig. 1 Study area. Gulf of Tonkin bathymetry from the GEBCO 2026 grid. Labelled are the tide-gauge stations used for validation (Hon Dau and Beihai, with Haikou, Dongfang and Vung Ang shown for context) and the study domain (red box). The Qiongzhou Strait lies at the northeastern corner, between Hainan and the Leizhou Peninsula, and the southern entrance opens to the South China Sea.

3 Data and methods

3.1 Datasets

Table 1 summarises the datasets. Tidal harmonic constants are taken from EOT20, an empirical ocean tide model derived from multi-mission satellite altimetry, which provides

amplitude and phase for seventeen constituents on a global 0.125° grid (Hart-Davis et al. 2021). Daily surface currents for calendar year 2020 come from the GLORYS12 global reanalysis at 1/12° resolution, distributed by the Copernicus Marine Service (Lellouche et al. 2018); this product does not include tidal forcing, and its daily averaging removes most tidal-band variance in any case, a point quantified in Sect. 4.6. Hourly total surface currents, in which tidal motion is represented through FES2014-based forcing (Lyard et al. 2021), were obtained from the CMEMS global operational system (SMOC merged product, cmems_mod_glo_phy_anfc_merged-uv_PT1H-i) for the earliest available continuous year, 1 November 2020 to 31 October 2021. Ten-metre winds for 2020 are from the ERA5 reanalysis (Hersbach et al. 2020). Bathymetry is taken from the GEBCO 2026 grid (GEBCO Bathymetric Compilation Group 2026). Hourly sea level at Hon Dau (20.67°N, 106.82°E; station 650) for 1995 was retrieved from the University of Hawaii Sea Level Center archive (Caldwell et al. 2015).

Table 1 Datasets used in this study

Dataset	Variables	Resolution	Period	Reference
EOT20	Tidal amplitude, phase (17 constituents)	0.125°	-	Hart-Davis et al. (2021)
GLORYS12 (CMEMS)	Daily surface u, v	1/12°	2020	Lellouche et al. (2018)
SMOC (CMEMS)	Hourly total surface u, v	1/12°	Nov 2020–Oct 2021	Lyard et al. (2021)
ERA5	10-m wind	0.25°	2020	Hersbach et al. (2020)
UHSLC (station 650)	Hourly sea level, Hon Dau	Station	1995	Caldwell et al. (2015)
UHSLC (station 636)	Hourly sea level, Beihai	Station	1997	Caldwell et al. (2015)
GEBCO 2026	Bathymetry	15 arcsec	-	GEBCO Bathymetric Compilation Group (2026)

3.2 Tidal regime classification

The tidal regime is classified with the Form Factor (Pugh and Woodworth 2014),

$$F = (A(K_1) + A(O_1)) / (A(M_2) + A(S_2)), \qquad (1)$$

where A denotes elevation amplitude. Values of F below 0.25 indicate a semi-diurnal regime, 0.25–1.5 mixed mainly semi-diurnal, 1.5–3 mixed mainly diurnal, and above 3 diurnal. Computing Eq. (1) on every ocean cell of the EOT20 grid yields a spatially continuous classification of the basin, which to our knowledge has not previously been published for the Gulf of Tonkin.

3.3 Barotropic scaling of tidal currents and power density

EOT20 supplies elevations only. To obtain a first-order current estimate we use the shallow-water progressive-wave relation,

$$U = A\eta \sqrt{(g/h)}, \qquad (2)$$

where $A\eta$ is the elevation amplitude of a constituent, g gravitational acceleration, and h the local depth from GEBCO. Equation (2) is exact for a freely propagating frictionless wave, in which velocity and elevation are in phase. We treat it here as a progressive-wave kinematic scaling of depth-averaged tidal current speed, interpreted as an order-of-magnitude estimate; its pointwise validity in a near-resonant standing-wave basin is assessed directly in Sect. 4.6. Hourly elevations and scaled currents were synthesised for calendar year 2020 from the major EOT20 constituents on the native grid. Mean surface power density was computed for both the scaled tidal currents and the reanalysis currents as

$$\bar{P} = \tfrac{1}{2}\,\rho\,\langle |U|^3 \rangle, \qquad (3)$$

with $\rho = 1025$ kg/m³ and angle brackets denoting the time mean. For reference against tidal-stream technology, we also count grid cells in which the synthesised maximum scaled speed reaches 0.5 m/s, a value near the cut-in speed of current turbine designs (Bahaj 2011; Lewis et al. 2015). The IEC technical specification for tidal resource characterisation (IEC 2015) requires far more than such first-order screening; we use the threshold only to delimit areas that could merit Stage-1 attention. Domain statistics in Sect. 4 are computed over the Gulf interior, 105.2–109.8°E, 18.2–22.3°N, the region shown in Fig. 7.

3.4 Validation against tide-gauge observations

Synthesised EOT20 elevations were compared with the hourly Hon Dau record for 1995, the longest continuous year available in the archive for this station. Hon Dau sits in the strongly diurnal northern Gulf and is the appropriate benchmark for this regime; stations south of the entrance, such as Vũng Tàu, lie in a mixed semi-diurnal environment and would not test the signal of interest. Agreement is quantified with the root-mean-square error (RMSE), the coefficient of determination R^2, the Nash–Sutcliffe efficiency (NSE), and the Willmott skill score. The nearest EOT20 ocean node lies roughly 15 km from the gauge, a separation that matters in an amphidromic gradient and is considered when interpreting the error statistics. The same comparison was repeated at a second, independent station in the diurnal north, Beihai (21.48°N, 109.08°E; UHSLC station 636) on the northern Chinese coast, using a complete year of hourly observations (1997); the two gauges span the head of the Gulf from 20.7° to 21.5°N and bracket the F = 3 isoline of the Form Factor map.

3.5 Constituent-level analysis of hourly currents

For constituent-level comparison between the tide-model scaling and realised tidal currents, the 365-day hourly SMOC record was extracted at four representative locations spanning the basin (P1, Qiongzhou Strait, 110.0°E 20.2°N; P2, northern Gulf, 107.8°E 20.5°N; P3, central Gulf, 107.3°E 18.5°N; P4, southern Gulf, 108.0°E 17.5°N) and analysed with the UTide implementation of classical harmonic analysis (Codiga 2011; Pawlowicz et al. 2002). Eight constituents (Q_1, O_1, P_1, K_1, N_2, M_2, S_2, K_2) are resolvable under the Rayleigh criterion at this record length, including the K_1/P_1 and S_2/K_2 pairs. The semi-major axis of each fitted current ellipse is the quantity compared with Eq. (2). The same hourly series, resampled to daily means before applying Eq. (3), quantifies how much tidal-band power density is removed by daily averaging.

3.6 Use of generative artificial intelligence

Analysis and figure-generation scripts were developed with the assistance of a large language model (Claude, Anthropic), which was also used for language editing. All methods, parameter choices, computations, and figures were specified, verified, and approved by the authors, who takes full responsibility for the content. All figures are data plots produced with Python from the datasets in Table 1; no generative-AI imagery was used.

4 Results

4.1 Validation at Hon Dau and Beihai

Figure 2 compares synthesised EOT20 elevations with the 1995 Hon Dau record; Table 2 lists the statistics. Three of the four metrics pass their conventional acceptance criteria: NSE = 0.916, R^2 = 0.928, and a Willmott skill of 0.980. The RMSE of 0.207 m exceeds the 0.15 m criterion. Given the ≈15 km separation between gauge and the nearest model node, the large local amplitude gradients of the northern Gulf, and the absence of any meteorological signal in the synthesis, we consider the agreement adequate for basin-scale characterisation: the model reproduces the timing and structure of the diurnal signal essentially without bias, and the residual is dominated by amplitude differences of order ten percent and by surge variance present in the gauge but not in the astronomical synthesis.

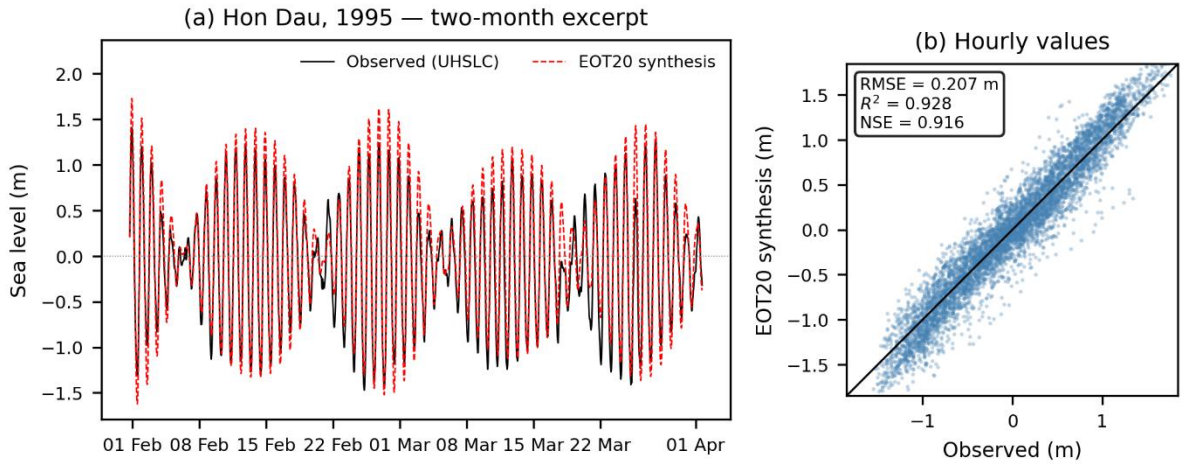

Fig. 2 Validation of the EOT20 harmonic synthesis against the hourly Hon Dau record, 1995: (a) two-month excerpt of observed and synthesised elevation, (b) scatter of synthesised against observed hourly values with the 1:1 line. Statistics in Table 2.

Table 2 Validation statistics, EOT20 synthesis versus Hon Dau hourly sea level, 1995

Metric	Value	Criterion	Outcome
RMSE (m)	0.207	< 0.15	not met
R^2	0.928	> 0.90	met
NSE	0.916	> 0.90	met
Willmott skill	0.980	> 0.90	met

Beyond the elevation time series, Table 3 sets the harmonic constants of the eight resolvable constituents at Hon Dau, from UTide analysis of the 1995 observations, against the EOT20 values interpolated to the station. The model follows the energetic diurnal constituents closely: K_1 and O_1 agree in amplitude to within 0.021 and 0.040 m, about three and five percent, and in Greenwich phase to 3.4 and 1.8 degrees. Amplitude agreement stays good for the weak semi-diurnal constituents, all below 0.07 m, though their phases drift as the amplitudes approach the noise floor of the altimetric solution in shallow water; the 35-degree phase offset of K_2, for instance, amounts to a vector difference of only 0.011 m. Summed over all eight constituents the root-mean-square vector difference is 0.070 m, 6.3 percent of the observed signal.

Repeating the comparison at Beihai (Table 4) gives the same picture at an independent site 90 km to the northeast. The diurnal amplitudes again match to within 0.044 m (K_1) and 0.054 m (O_1), and every constituent agrees in phase to better than four degrees, the M_2 phase to a tenth of a degree. The vector difference is 0.113 m, 7.3 percent of the observed signal. Tides at Beihai are stronger than at Hon Dau, the O_1 semi-major amplitude reaching 1.03 m, and EOT20 underestimates them slightly but consistently, as expected where an altimetric model resolves shallow coastal water least well. A Form Factor of 3.2 computed directly from the Beihai record places the station just inside the diurnal class and confirms, from observations alone, the F = 3 isoline mapped in Sect. 4.2. Taken together the two gauges show that the synthesis captures the diurnal tide across the head of the basin to within seven percent in combined amplitude and phase.

Table 3 Harmonic constants at Hon Dau: UTide analysis of the 1995 observations versus EOT20 interpolated to the station. Amplitudes A in metres, Greenwich phase lags g in degrees; Δg = g(EOT20) − g(obs); vector difference D = |Z_obs − Z_EOT20| with Z = A e^(−ig).

Const.	A_obs (m)	A_EOT20 (m)	g_obs (°)	g_EOT20 (°)	Δg (°)	D (m)
K_1	0.710	0.688	345.9	342.5	−3.4	0.047
O_1	0.810	0.771	290.1	288.3	−1.8	0.047
P_1	0.233	0.221	341.0	338.2	−2.8	0.017
Q_1	0.161	0.157	260.3	259.0	−1.2	0.005
M_2	0.064	0.062	198.3	201.1	+2.8	0.004
S_2	0.047	0.046	253.6	244.8	−8.8	0.007
N_2	0.007	0.010	240.1	229.9	−10.2	0.003
K_2	0.019	0.018	221.8	256.8	+35.0	0.011
RSS	-	-	-	-	-	0.070

Table 4 Harmonic constants at Beihai (UHSLC station 636): UTide analysis of the 1997 observations versus EOT20 interpolated to the station. Columns as in Table 3. Observed Form Factor F = 3.2.

Const.	A_obs (m)	A_EOT20 (m)	g_obs (°)	g_EOT20 (°)	Δg (°)	D (m)
K_1	0.950	0.906	335.4	336.5	+1.0	0.046
O_1	1.034	0.980	280.5	282.3	+1.8	0.063
P_1	0.290	0.282	330.2	334.0	+3.7	0.021
Q_1	0.206	0.197	252.7	254.0	+1.4	0.011
M_2	0.507	0.439	307.6	307.7	+0.1	0.068
S_2	0.117	0.092	356.8	358.2	+1.4	0.025
N_2	0.097	0.085	279.3	279.8	+0.4	0.012
K_2	0.096	0.068	17.4	14.5	−2.9	0.028
RSS	-	-	-	-	-	0.113

4.2 A spatially continuous Form Factor map

Figure 3 presents the Form Factor field computed from Eq. (1). The F = 3 contour, separating diurnal from mixed regimes, crosses the basin near 19°N. North of it the entire Gulf interior is diurnal, with F rising to a maximum of 12.7; the classification only relaxes to mixed mainly diurnal in the far south, approaching the open South China Sea. The map gives spatial form to what station harmonic constants have long implied (Fang et al. 1999; Minh et al. 2014): diurnal dominance is not a coastal peculiarity of the Hải Phòng area but the condition of essentially the whole northern basin. Constituent amplitude maps (Fig. 4) show the familiar structure behind this: K_1 and O_1 amplify toward the head of the Gulf, exceeding 0.8 m, while M_2 remains below 0.25 m through most of the interior with an amphidromic minimum in the north.

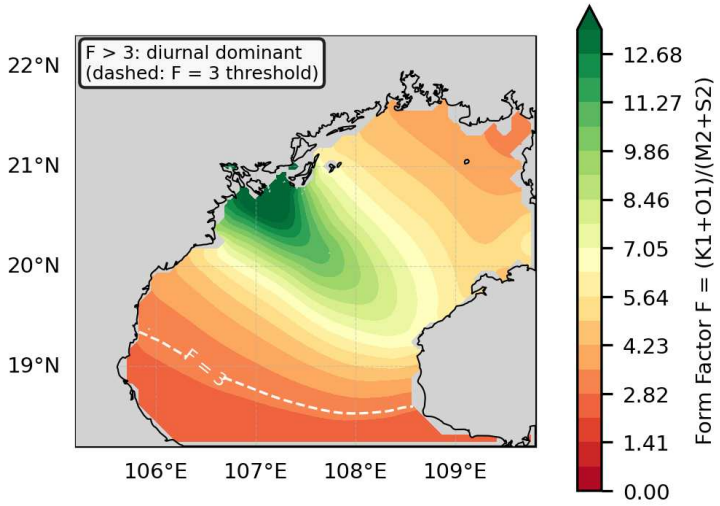

Fig. 3 Spatially continuous Form Factor map of the Gulf of Tonkin computed from EOT20 amplitudes (Eq. 1). The heavy contour marks F = 3, the boundary of the diurnal regime; F reaches 12.7 in the northern interior.

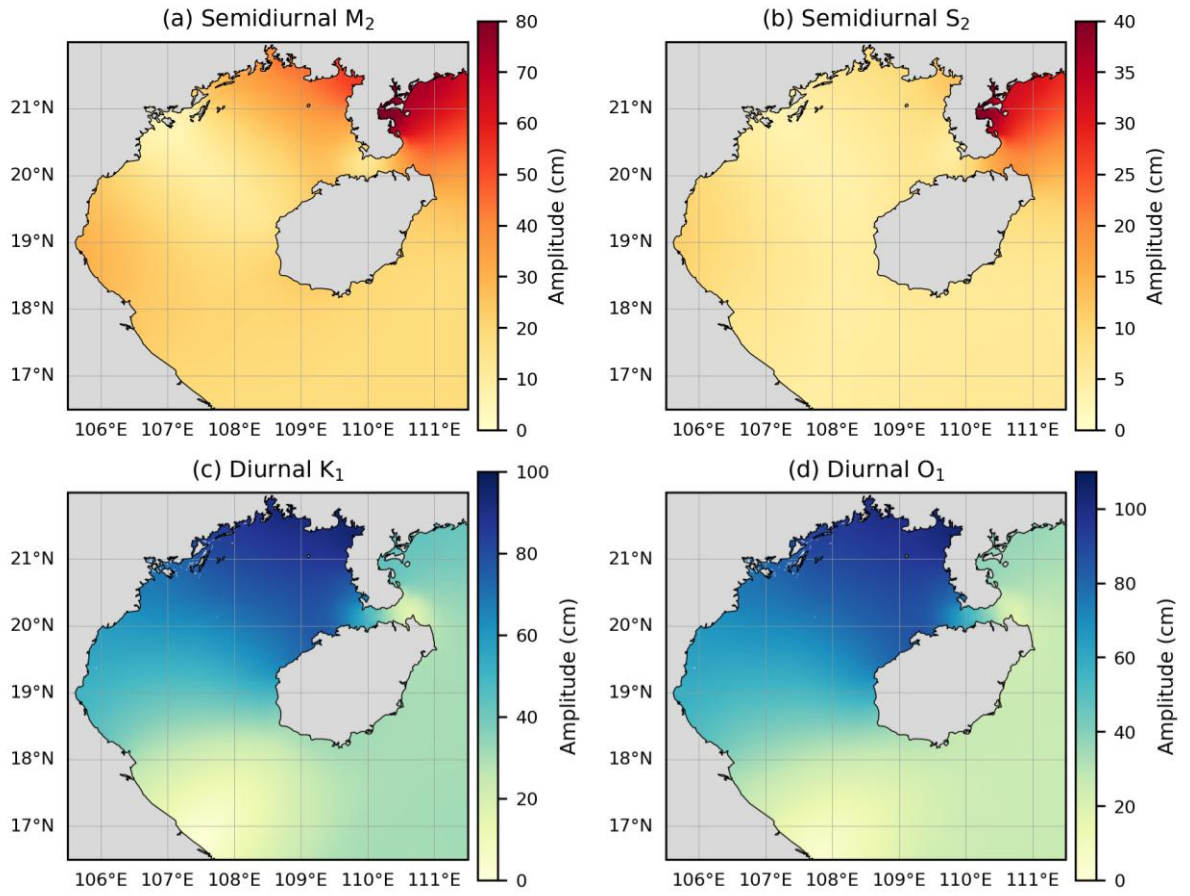

Fig. 4 Elevation amplitudes (cm) of the four principal constituents from EOT20: (a) M_2, (b) S_2, (c) K_1, (d) O_1.

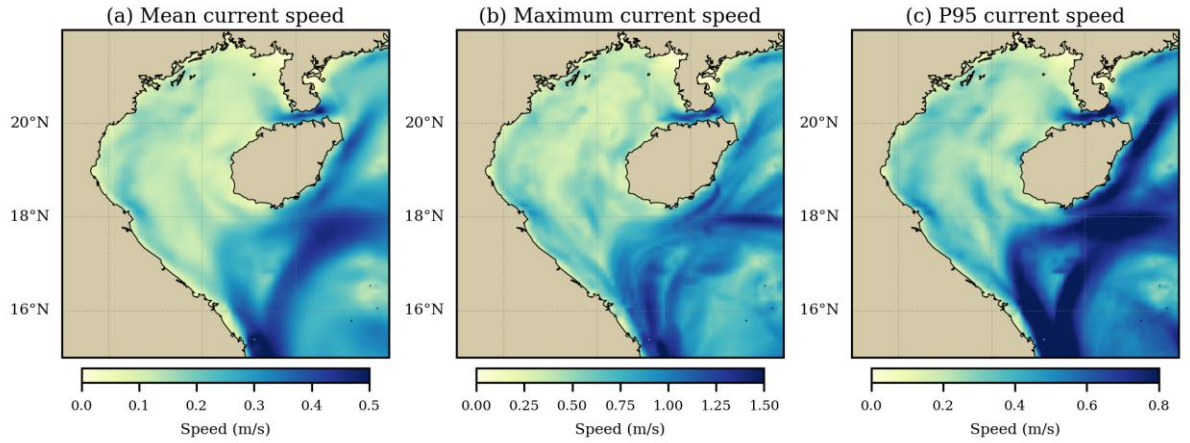

Fig. 5 Surface current statistics from the GLORYS12 daily reanalysis, 2020: (a) mean speed, (b) maximum speed, (c) 95th-percentile speed.

4.3 Surface currents and power density in the daily reanalysis

The GLORYS12 daily surface currents for 2020 (Fig. 5) show a circulation dominated by the monsoon-driven coastal flow along Vietnam and by exchange near the two openings. Mean power density computed with Eq. (3) is 2.86 W/m² over the basin, with a maximum of 44.99 W/m²; the highest values hug the southwestern coast and the entrance. Seasonally (Fig. 6), the reanalysis peaks in autumn (SON) at 4.37 W/m², coinciding with the onset of the

northeast monsoon and the spin-up of the southward coastal jet (Gao et al. 2013). These values describe the slowly varying circulation: as shown in Sect. 4.6, the daily averaging underlying this product removes most tidal-band kinetic energy before Eq. (3) is applied.

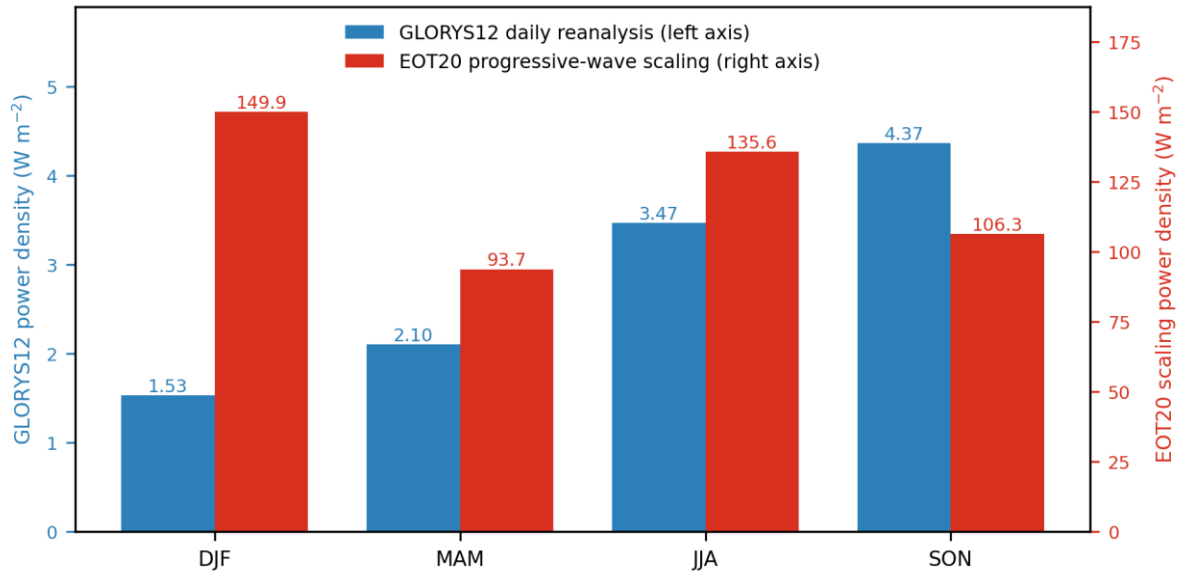

Fig. 6 Seasonal cycle of domain-mean surface power density, 2020, over the statistics domain (105.2–109.8°E, 18.2–22.3°N): GLORYS12 daily reanalysis (left axis; autumn maximum, 4.37 W/m² in SON) and the EOT20 progressive-wave scaling (right axis; winter maximum, 149.9 W/m² in DJF). The two products use separate axes because their domain means differ by more than an order of magnitude.

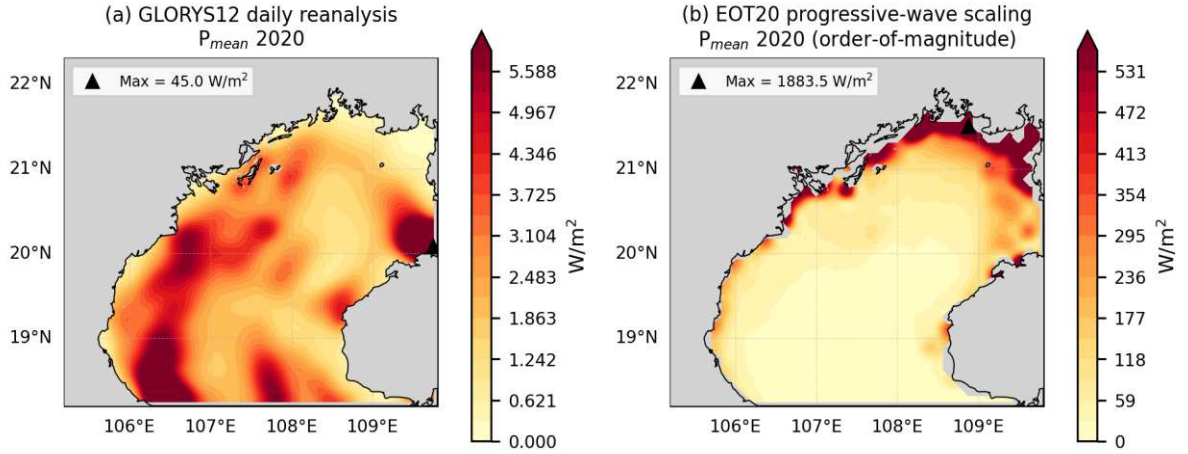

Fig. 7 Mean surface power density (W/m²), 2020, over the statistics domain (105.2–109.8°E, 18.2–22.3°N): (a) GLORYS12 daily reanalysis currents, (b) progressive-wave scaling of the EOT20 tide (Eqs. 2–3), an order-of-magnitude kinematic estimate rather than a pointwise bound. Colour scales are independent and saturate at each field's 95th percentile; triangles mark the field maxima.

4.4 Tidal power density from the EOT20 scaling and the Qiongzhou hotspot

Applying Eqs. (2)–(3) to the synthesised 2020 tide gives a very different field (Fig. 7). The domain mean is 121.35 W/m² and the interior maximum 1,884 W/m², concentrated where large diurnal elevation amplitudes meet shallow water. In 551 grid cells the synthesised maximum scaled speed reaches 0.5 m/s. The most prominent feature is a hotspot at the western approach to the Qiongzhou Strait, centred near 20.08°N, 109.75°E (Fig. 8), consistent with the

strong tidal exchange known to pass through the channel (Shi et al. 2002). The seasonal cycle of the scaled tidal power (Fig. 6) peaks in winter (DJF) at 149.9 W/m², with a secondary maximum in summer (135.6 W/m² in JJA), reflecting the semi-annual modulation of the declinational diurnal tides, whose tropic ranges maximise near the solstices.

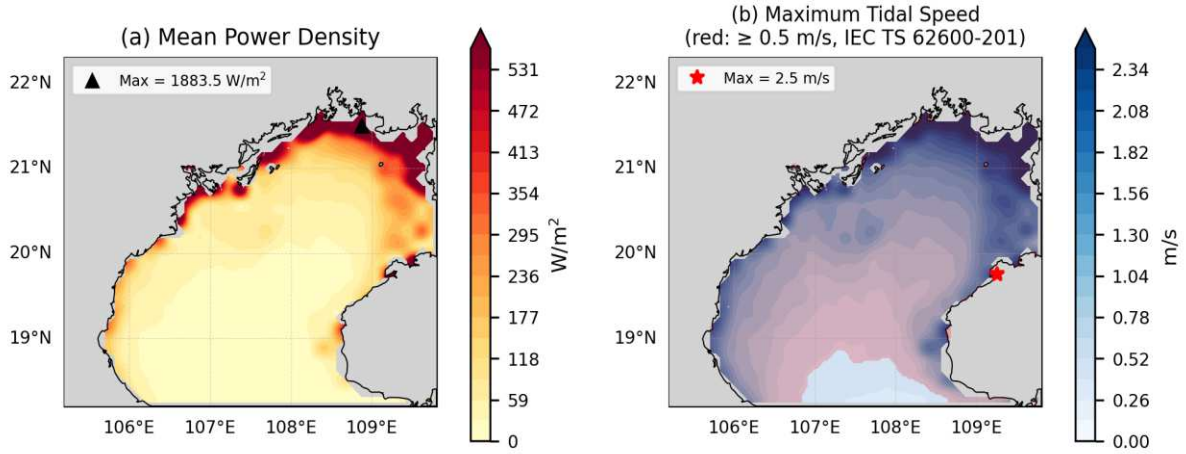

Fig. 8 Tidal-stream screening from the EOT20 scaling: cells with synthesised maximum speed ≥ 0.5 m/s (551 cells) and the hotspot at the western approach to the Qiongzhou Strait (20.08°N, 109.75°E). Synthesised speeds are capped at 2.5 m/s.

4.5 Multi-source comparison

Table 5 sets the two estimates side by side. The domain-mean power densities differ by a factor of about 42, and the spatial patterns differ as much as the magnitudes: the reanalysis concentrates energy along the monsoon-driven western boundary, the tidal scaling in the shallow north and at the strait. The two products are complementary descriptions of different parts of the velocity spectrum rather than competing estimates of one quantity. The constituent-level analysis of Sect. 4.6 shows, however, that the EOT20-based scaling is not a pointwise upper bound: its relationship to the realised tidal currents is spatially structured by the standing-wave character of the diurnal oscillation.

Table 5 Domain statistics of mean surface power density, 2020

Product	Mean (W/m²)	Max (W/m²)	Cells ≥ 0.5 m/s
GLORYS12 daily reanalysis	2.86	44.99	-
EOT20 progressive-wave scaling	121.35	1,884	551

4.6 Tidal constituent separation from CMEMS surface currents

The domain-average comparison in Sect. 4.5 contrasts two physically distinct quantities, and the daily temporal resolution of the reanalysis used in Sect. 4.3 removes most of the tidal oscillation before kinetic energy is computed. To examine the tidal signal directly, we apply UTide harmonic analysis to the hourly SMOC total surface currents described in Sect. 3.5, at the four representative locations P1–P4 (Fig. 9a). The 365-day record resolves eight constituents under the Rayleigh criterion, and the semi-major axis of each tidal current ellipse

is compared with the progressive-wave scaling of Eq. (2) evaluated from the EOT20 elevation amplitude and the GEBCO depth at the same location.

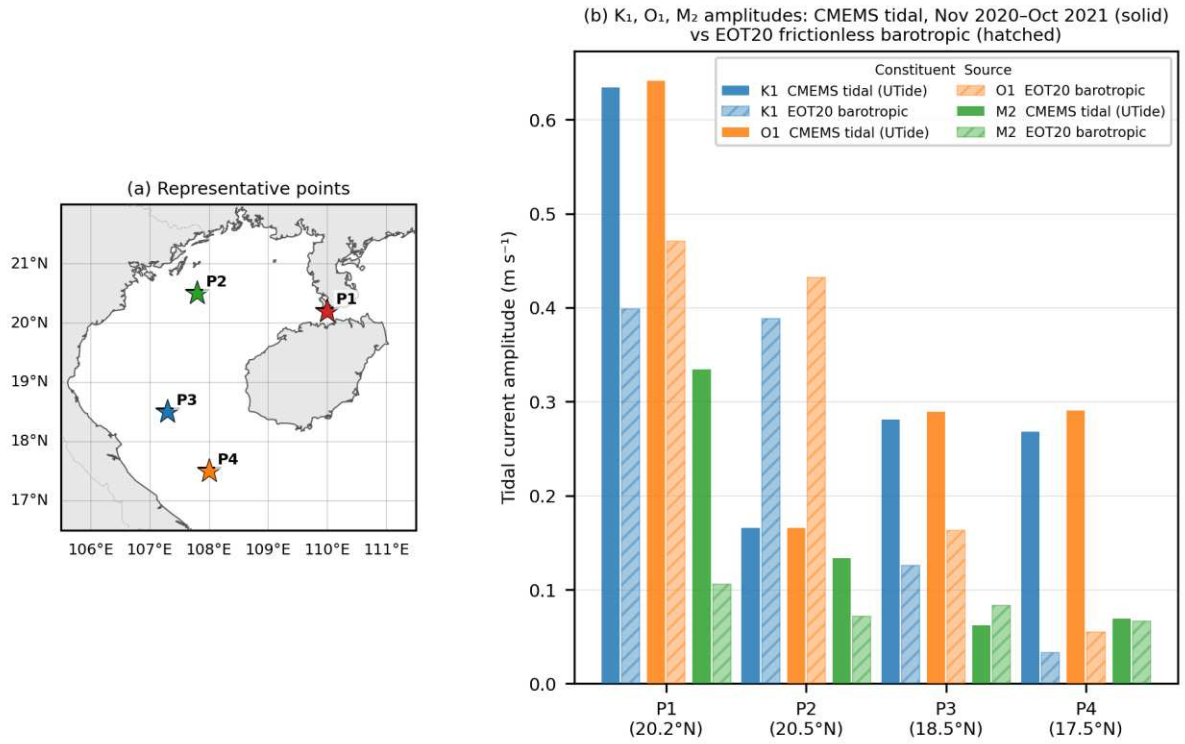

Fig. 9 Tidal constituent amplitude comparison at four representative locations (P1–P4). (a) Location of the points. (b) Semi-major axis amplitudes for K_1, O_1 and M_2: solid bars, tidal amplitudes extracted from hourly CMEMS SMOC total surface currents by UTide harmonic analysis (1 Nov 2020–31 Oct 2021); hatched bars, progressive-wave estimates from EOT20 elevation amplitudes and GEBCO 2026 depths (Eq. 2).

At all four sites the K_1 and O_1 semi-major axes exceed M_2 (Table 6; Fig. 9b), providing direct kinematic confirmation of the diurnal regime mapped in Sect. 4.2. Diurnal current amplitudes range from 0.165 to 0.634 m/s for K_1 and 0.166 to 0.641 m/s for O_1, with the strongest values at the Qiongzhou Strait (P1), where the combined diurnal amplitude approaches 1.3 m/s, consistent with the hotspot of Sect. 4.4. The ratio between the EOT20 scaling and the extracted tidal amplitude, however, spans 0.1–2.6 and is spatially structured rather than uniformly greater than unity. The scaling exceeds the harmonic amplitudes only at P2, adjacent to the northern elevation antinode ($A\eta$ = 0.73–0.82 m for K_1 and O_1), and falls to 0.1–0.2 at P4 near the southern entrance, where elevation amplitudes are smallest (0.10–0.17 m) but tidal currents remain substantial.

This pattern follows directly from the standing-wave character of the near-resonant diurnal oscillation of the Gulf (Piton et al. 2020). Equation (2) assumes a freely propagating wave in which velocity and elevation are in phase and proportional. In a quarter-wavelength resonator, by contrast, velocity maxima occur near the nodal region at the basin entrance where elevation amplitudes are smallest, while the antinodal head combines large elevations with weak currents. The spatial distribution of the ratio in Table 6 therefore diagnoses the standing-wave structure of the diurnal tide rather than frictional attenuation alone, and demonstrates that

the barotropic scaling must be interpreted as an order-of-magnitude kinematic estimate, not a pointwise upper bound on tidal current speed. The additional exceedance of the local scaling at P1 reflects continuity-driven amplification through the constricted Qiongzhou Strait, a channel process the pointwise formula cannot represent (Garrett and Cummins 2005). We note that the SMOC tidal currents derive from FES2014 forcing within an operational model, so this is a comparison between dynamically consistent model products rather than independent observations, and the SMOC field is a surface velocity whereas the scaling targets the depth average.

A second, independent factor separates the EOT20-based and reanalysis-based energy estimates: temporal resolution. Resampling the hourly SMOC record to daily means and recomputing Eq. (3) reduces the mean surface power density by factors of 3.8–8.9 across the four sites (mean 6.4; Table 7), because daily averaging removes most of the diurnal and semi-diurnal velocity variance before the cubic operation. The daily reanalysis fields of Sect. 4.3 are therefore intrinsically incapable of representing tidal-band kinetic energy. Combined with the cubic sensitivity of Eq. (3) to the shallow-water overestimates of the scaling, which dominate the domain average through the $\sqrt{(g/h)}$ factor in the extensive shallow northern Gulf, these two effects account for the approximately 42-fold domain-average discrepancy of Sect. 4.5 without invoking a pointwise frictionless ceiling.

Table 6 Tidal constituent amplitude comparison at four representative locations. CMEMS tidal: semi-major axis extracted by UTide from hourly SMOC total surface currents (1 Nov 2020–31 Oct 2021). EOT20 scaling: Eq. (2) with EOT20 elevation amplitude and GEBCO 2026 depth. Ratio = scaling / CMEMS tidal

Location	Const.	h (m)	CMEMS tidal (m/s)	EOT20 scaling (m/s)	Ratio
P1 - Qiongzhou Strait	K_1	13	0.634	0.399	0.6
	O_1		0.641	0.471	0.7
	M_2		0.334	0.106	0.3
P2 - Northern Gulf	K_1	35	0.165	0.388	2.3
	O_1		0.166	0.432	2.6
	M_2		0.133	0.072	0.5
P3 - Central Gulf	K_1	66	0.281	0.126	0.4
	O_1		0.289	0.163	0.6
	M_2		0.062	0.083	1.3
P4 - Southern Gulf	K_1	89	0.268	0.033	0.1
	O_1		0.291	0.055	0.2
	M_2		0.069	0.067	1.0

Table 7 Effect of temporal averaging on mean surface power density at P1–P4, computed from the same hourly SMOC record before and after resampling to daily means

Location	$\bar{P}$ hourly (W/m²)	$\bar{P}$ daily-mean (W/m²)	Ratio
P1 - Qiongzhou Strait	483.3	56.5	8.6
P2 - Northern Gulf	17.9	4.7	3.8
P3 - Central Gulf	38.9	4.4	8.9
P4 - Southern Gulf	50.3	11.2	4.5
Mean	-	-	6.4

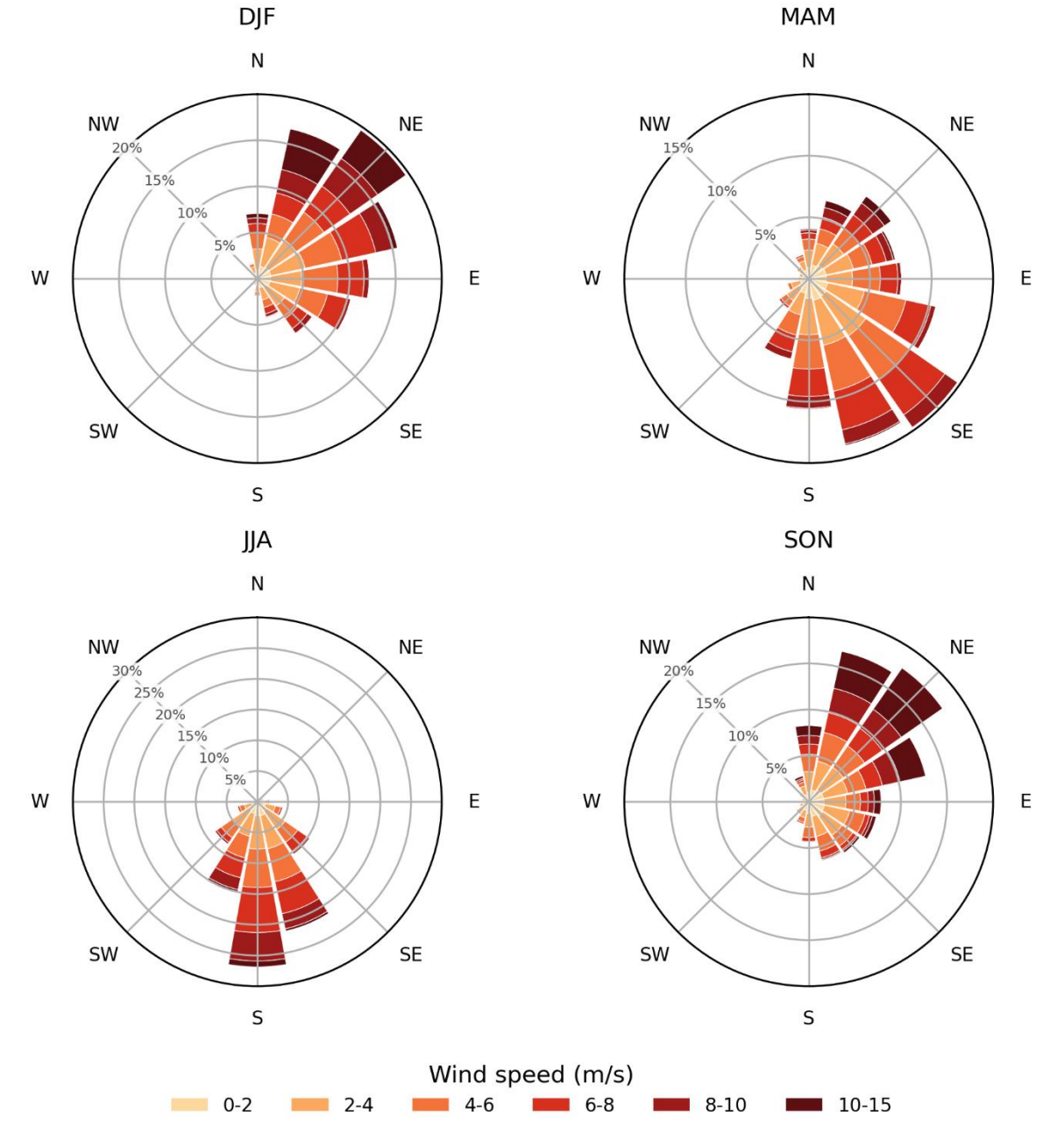

Fig. 10 Seasonal wind climatology over the Gulf of Tonkin from ERA5 10-m winds, 2020: wind roses for DJF, MAM, JJA, and SON. Petal length gives the percentage of hourly observations with wind blowing from each direction sector; colours give the wind-speed class (m/s).

4.7 Seasonal variability

The two products place their seasonal maxima in different seasons for different physical reasons (Fig. 6). The reanalysis power density peaks in autumn (4.37 W/m² in SON) with the onset of the northeast monsoon (Fig. 10) and the acceleration of the coastal current along Vietnam; a secondary maximum occurs in summer under the southwest monsoon (3.47 W/m² in JJA), while winter and spring are weakest (1.53 and 2.10 W/m²). The scaled tidal power peaks in winter (149.9 W/m² in DJF) with a secondary summer maximum (135.6 W/m² in JJA), following the semi-annual cycle of the declinational diurnal constituents. The seasonal cycles are thus out of phase by roughly one season, and any application sensitive to within-year variability, from sediment transport to energy yield, will reach different conclusions depending on which component of the flow controls it.

5 Discussion

5.1 What sustains diurnal dominance

The Form Factor map of Sect. 4.2 and the constituent ellipses of Sect. 4.6 describe the same dynamics from two directions. The Gulf behaves as a quarter-wavelength oscillator whose natural period lies close to one day, so the K_1 and O_1 waves entering from the South China Sea are resonantly amplified while M_2, far from resonance, propagates through with an interior amphidrome and little amplification (Fang et al. 1999; Zu et al. 2008; Minh et al. 2014; Piton et al. 2020). The kinematic consequence, documented here for the first time at constituent level from a year of hourly currents, is that the velocity and elevation fields of the diurnal tide are spatially complementary: currents peak near the nodal entrance and in the strait, elevations at the antinodal head.

The resonance can be made quantitative with a first-order Merian estimate. Treating the Gulf as a semi-enclosed basin open at its southern entrance, the gravest quarter-wavelength mode has period $T = 4L/\sqrt{(gh)}$ for along-gulf length L and mean depth h. With $L \approx 500$ km and $h \approx 50$ m this gives $T \approx 25$ h, between K_1 (23.93 h) and O_1 (25.82 h); over plausible bounds (L = 450–550 km, h = 45–55 m) T stays within 21.5–29 h, so the diurnal constituents remain near resonance throughout, whereas M_2 (12.42 h), at almost exactly half the resonant period, sits far from it. The basin amplifies the incoming diurnal waves while passing the semi-diurnal tide with little gain, the behaviour found in detailed modelling of the Gulf (Fang et al. 1999; Zu et al. 2008; Piton et al. 2020). The quarter-wavelength geometry also explains the spatial pattern of Sect. 4.6 directly: a standing wave places its elevation antinode at the closed northern head, where currents are weak (point P2), and its velocity antinode near the open southern entrance, where elevations are small but currents strong (point P4). The mode inferred kinematically from the hourly currents and the resonant period derived here are two views of the same oscillation.

A near-resonant diurnal response is not peculiar to the Gulf of Tonkin. The neighbouring Gulf of Thailand, a comparably shallow basin of the same South China Sea system, is diurnal-dominant for the same reason (Fang et al. 1999), and other shallow gulfs whose gravest resonant period nears one day show the same selective amplification of K_1 and

O_1. What sets the Gulf of Tonkin apart is the combination of an unusually clean diurnal regime, mapped here as a continuous field, with the strong currents the resonance drives through the shallow north and the Qiongzhou Strait.

5.2 The standing wave controls the elevation-to-velocity scaling

A practical lesson follows for anyone estimating currents from a tide model in a resonant basin. The progressive-wave relation of Eq. (2) is the natural first-order conversion and is widely used in screening studies, but in the Gulf of Tonkin its pointwise error is not a modest frictional correction: it overestimates by a factor of about 2.5 near the elevation antinode and underestimates by up to a factor of ten near the node (Table 6). The sign and size of the error map the standing-wave structure, so the ratio itself carries physical information. Domain-integrated quantities inherit the bias asymmetrically, because Eq. (3) cubes the velocity and the $\sqrt{(g/h)}$ factor inflates precisely the shallow antinodal regions that occupy most of the northern Gulf. Together with the 6.4-fold average suppression of tidal-band power by daily averaging (Table 7), this explains the apparent 42-fold discrepancy of Sect. 4.5 quantitatively and without contradiction.

5.3 Monsoon and tide as complementary energy reservoirs

The reanalysis and the tidal synthesis are best read as descriptions of two reservoirs of surface kinetic energy that coexist in the basin. The monsoon-driven reservoir is broad, slowly varying, strongest along the western boundary, and peaks in autumn; the tidal reservoir is concentrated in the shallow north and the Qiongzhou approach, oscillates at diurnal frequency, and peaks in winter (Hu et al. 2000; Gao et al. 2013; Tran et al. 2021). High-frequency radar observations in the western Gulf support this partition, showing tidal and subtidal variance of comparable importance with distinct spatial structure (Tran et al. 2021).

5.4 Implications for navigation and port operations

The tidal characterisation carries direct consequences for shipping in the Gulf, which moves heavy traffic to the port of Hải Phòng and through the Qiongzhou Strait. Two features stand out. First, the diurnal regime sets the rhythm of access to the shallow northern ports. Because K_1 and O_1 dominate, the Gulf sees essentially one high water and one low water each day rather than the two of a semi-diurnal regime, so the tidal window for deep-draft vessels at the head of the basin - where the range exceeds 4 m at tropic tides - opens once daily rather than twice. Modulated fortnightly by the tropic–equatorial cycle rather than the spring–neap cycle familiar from semi-diurnal seas (Sect. 4.7), this single window is a tighter scheduling constraint than masters accustomed to semi-diurnal ports may anticipate. Second, the standing-wave structure concentrates the strongest tidal currents in the Qiongzhou Strait, the narrow channel between Hainan and the mainland, where the combined diurnal amplitude approaches 1.3 m/s, about 2.5 knots, and reverses on the diurnal cycle. In a constricted lane such currents bear directly on transit timing, set and drift, and under-keel clearance, and the slack-water windows for safe passage recur once a day rather than twice. The harmonic constants validated in Tables 3 and 4, together with the continuous Form Factor field, supply the constituent basis from which these windows can be predicted for tide tables and tidal-stream guidance (Pugh and Woodworth 2014).

5.5 Implications for tidal-stream energy screening

For energy applications the message is twofold. First, daily reanalysis products are unsuitable for tidal-stream screening anywhere, not because they are inaccurate but because their averaging removes the resource: at our four sites the hourly record carries four to nine times the power density of its own daily means. Hourly products with explicit tidal forcing, or harmonic synthesis validated against gauges, are the appropriate starting point. Second, within the Gulf only the Qiongzhou Strait approach combines current amplitudes near technological cut-in speeds with proximity to demand; combined diurnal amplitudes of 1.3 m/s at P1, and the channel amplification that the pointwise scaling cannot capture, mark it as the single area worth a Stage-1 assessment in the sense of IEC (2015). The diurnal character of the resource also matters for yield: a diurnal regime delivers one, not two, energetic exceedance windows per day, with a pronounced fortnightly tropic–equatorial cycle rather than the familiar spring–neap cycle of semi-diurnal seas (Lewis et al. 2015; Robins et al. 2015).

5.6 Limitations

Several caveats bound these conclusions. The constituent comparison of Sect. 4.6 is between model-consistent products: SMOC tidal motion derives from FES2014, not from independent current observations, and the SMOC field is a surface velocity while Eq. (2) targets the depth average. The analysis covers a single year and four locations; interannual variability and the 18.6-year nodal modulation of the diurnal constituents are not sampled. EOT20, like all altimetric models, is least accurate in shallow coastal water, exactly where the Gulf's amplitudes are largest, and the 15-km gauge–node separation at Hon Dau contributes to the RMSE exceedance in Table 2. Finally, the depth entering Eq. (2) at the strait point P1 (13 m in GEBCO) may not represent the effective channel cross-section. In-situ current measurements and a tide-resolving regional model, planned as the next stage of this work, are the natural tests of the standing-wave interpretation advanced here.

6 Conclusions

From a multi-source analysis built entirely on open global products, the main conclusions are as follows.

1. The first spatially continuous Form Factor map of the Gulf of Tonkin confirms that diurnal dominance is a basin-scale condition rather than a coastal peculiarity: the F = 3 contour crosses the Gulf near 19°N and F reaches 12.7 in the northern interior.

2. EOT20 harmonic synthesis reproduces the hourly records at Hon Dau (1995) and Beihai (1997) with NSE = 0.916 and a Willmott skill of 0.980 at Hon Dau, and constituent amplitudes matching to within six to seven percent in vector terms at both stations. The 0.207 m RMSE at Hon Dau mainly reflects the 15-km gauge-to-node separation and surge variance absent from the astronomical synthesis.

3. Mean surface power density from the daily GLORYS12 reanalysis (2.86 W/m²) and from a frictionless progressive-wave scaling of the EOT20 tide (121.35 W/m²) differ by a factor of about 42, but this gap is not a pointwise frictional ratio. Daily averaging alone suppresses tidal-band power density by factors of 3.8–8.9 (mean 6.4), and the cubic

dependence of power on velocity amplifies the shallow-water overestimates of the √(g/h) scaling in the domain mean.

4. At constituent level, the ratio between the scaling and the realised tidal amplitudes (0.1–2.6) is organised by the standing-wave structure of the near-resonant diurnal oscillation: the scaling overestimates currents near the elevation antinode of the northern Gulf (2.3–2.6× at P2) and underestimates them near the nodal entrance (0.1–0.2× at P4) and in the Qiongzhou Strait. Progressive-wave kinematics should therefore not be applied pointwise to convert altimetric tide models to currents in resonant basins.

5. K_1 and O_1 current amplitudes exceed M_2 at every site analysed, with a combined diurnal amplitude approaching 1.3 m/s at the western approach to the Qiongzhou Strait - a busy shipping lane where these currents bear on transit timing and under-keel clearance, and the only part of the Gulf where first-order screening thresholds for tidal-stream energy are met and a Stage-1 assessment in the sense of IEC (2015) appears justified.

6. Daily-mean current products are unsuitable for any tidal-band energy estimate, in the Gulf of Tonkin or elsewhere. Hourly products with explicit tidal forcing, or harmonic synthesis validated against tide gauges, are the appropriate starting point for resource screening.

Statements and Declarations

Funding This research received no external funding.

Competing interests The author declares no competing interests.

Data availability All datasets are openly available: EOT20 from SEANOE (https://doi.org/10.17882/79489); GLORYS12 daily currents (GLOBAL_MULTIYEAR_PHY_001_030) and hourly SMOC surface currents (cmems_mod_glo_phy_anfc_merged-uv_PT1H-i, https://doi.org/10.48670/moi-00016) from the Copernicus Marine Service; ERA5 from the Copernicus Climate Data Store (https://doi.org/10.24381/cds.adbb2d47); tide-gauge records from the University of Hawaii Sea Level Center (https://doi.org/10.7289/V5V40S7W); bathymetry from GEBCO (https://www.gebco.net). Analysis scripts are available from the author on reasonable request.

References

Bahaj AS (2011) Generating electricity from the oceans. Renew Sustain Energy Rev 15(7):3399–3416. https://doi.org/10.1016/j.rser.2011.04.032

Caldwell PC, Merrifield MA, Thompson PR (2015) Sea level measured by tide gauges from global oceans - the Joint Archive for Sea Level holdings (NCEI Accession 0019568). NOAA National Centers for Environmental Information, Dataset. https://doi.org/10.7289/V5V40S7W

Codiga DL (2011) Unified tidal analysis and prediction using the UTide Matlab functions. Technical Report 2011-01, Graduate School of Oceanography, University of Rhode Island, Narragansett. https://doi.org/10.13140/RG.2.1.3761.2008

Egbert GD, Erofeeva SY (2002) Efficient inverse modeling of barotropic ocean tides. J Atmos Ocean Technol 19(2):183–204. https://doi.org/10.1175/1520-0426(2002)019<0183:EIMOBO>2.0.CO;2

Fang G, Kwok Y-K, Yu K, Zhu Y (1999) Numerical simulation of principal tidal constituents in the South China Sea, Gulf of Tongking and Gulf of Thailand. Cont Shelf Res 19(7):845–869. https://doi.org/10.1016/S0278-4343(99)00002-3

Gao J, Xue H, Chai F, Shi M (2013) Modeling the circulation in the Gulf of Tonkin, South China Sea. Ocean Dyn 63(8):979–993. https://doi.org/10.1007/s10236-013-0636-y

Garrett C, Cummins P (2005) The power potential of tidal currents in channels. Proc R Soc A 461(2060):2563–2572. https://doi.org/10.1098/rspa.2005.1494

GEBCO Bathymetric Compilation Group (2026) The GEBCO_2026 Grid - a continuous terrain model for oceans and land at 15 arc-second intervals. NERC EDS British Oceanographic Data Centre NOC. https://doi.org/10.5285/4f68d5c7-45eb-f999-e063-7086abc036fa

Hart-Davis MG, Piccioni G, Dettmering D, Schwatke C, Passaro M, Seitz F (2021) EOT20: a global ocean tide model from multi-mission satellite altimetry. Earth Syst Sci Data 13(8):3869–3884. https://doi.org/10.5194/essd-13-3869-2021

Hersbach H, Bell B, Berrisford P, et al (2020) The ERA5 global reanalysis. Q J R Meteorol Soc 146(730):1999–2049. https://doi.org/10.1002/qj.3803

Hu J, Kawamura H, Hong H, Qi Y (2000) A review on the currents in the South China Sea: seasonal circulation, South China Sea Warm Current and Kuroshio intrusion. J Oceanogr 56(6):607–624. https://doi.org/10.1023/A:1011117531252

IEC (2015) Marine energy - Wave, tidal and other water current converters - Part 201: Tidal energy resource assessment and characterization. IEC TS 62600-201:2015, International Electrotechnical Commission, Geneva

Lellouche J-M, Greiner E, Le Galloudec O, et al (2018) Recent updates to the Copernicus Marine Service global ocean monitoring and forecasting real-time 1/12° high-resolution system. Ocean Sci 14(5):1093–1126. https://doi.org/10.5194/os-14-1093-2018

Lewis M, Neill SP, Robins PE, Hashemi MR (2015) Resource assessment for future generations of tidal-stream energy arrays. Energy 83:403–415. https://doi.org/10.1016/j.energy.2015.02.038

Lyard FH, Allain DJ, Cancet M, Carrère L, Picot N (2021) FES2014 global ocean tide atlas: design and performance. Ocean Sci 17(3):615–649. https://doi.org/10.5194/os-17-615-2021

Minh NN, Marchesiello P, Lyard F, Ouillon S, Cambon G, Allain D, Dinh VU (2014) Tidal characteristics of the Gulf of Tonkin. Cont Shelf Res 91:37–56. https://doi.org/10.1016/j.csr.2014.08.003

Pawlowicz R, Beardsley B, Lentz S (2002) Classical tidal harmonic analysis including error estimates in MATLAB using T_TIDE. Comput Geosci 28(8):929–937. https://doi.org/10.1016/S0098-3004(02)00013-4

Piton V, Herrmann M, Lyard F, Marsaleix P, Duhaut T, Allain D, Ouillon S (2020) Sensitivity study on the main tidal constituents of the Gulf of Tonkin by using the frequency-domain tidal solver in T-UGOm. Geosci Model Dev 13(3):1583–1607. https://doi.org/10.5194/gmd-13-1583-2020

Pugh D, Woodworth P (2014) Sea-Level Science: Understanding Tides, Surges, Tsunamis and Mean Sea-Level Changes. Cambridge University Press, Cambridge. https://doi.org/10.1017/CBO9781139235778

Robins PE, Neill SP, Lewis MJ, Ward SL (2015) Characterising the spatial and temporal variability of the tidal-stream energy resource over the northwest European shelf seas. Appl Energy 147:510–522. https://doi.org/10.1016/j.apenergy.2015.03.045

Shi M, Chen C, Xu Q, Lin H, Liu G, Wang H, Wang F, Yan J (2002) The role of Qiongzhou Strait in the seasonal variation of the South China Sea circulation. J Phys Oceanogr 32(1):103–121. https://doi.org/10.1175/1520-0485(2002)032<0103:TROQSI>2.0.CO;2

Tran MC, Sentchev A, Nguyen KC (2021) Multi-scale variability of circulation in the Gulf of Tonkin from remote sensing of surface currents by high-frequency radars. Ocean Dyn 71:175–194. https://doi.org/10.1007/s10236-020-01440-x

Zu T, Gan J, Erofeeva SY (2008) Numerical study of the tide and tidal dynamics in the South China Sea. Deep-Sea Res Part I 55(2):137–154. https://doi.org/10.1016/j.dsr.2007.10.007

Supplementary Files

This is a list of supplementary files associated with this preprint. Click to download.

- TableforOD1stsubmission.docx